Materials and Design 89 (2016) 1095–1106

Contents lists available at ScienceDirect

Materials and Design

journal homepage: www.elsevier.com/locate/jmad

Water droplet erosion mechanism of nearly fully-lamellar gamma TiAl alloy

M.S. Mahdipoor [a], D. Kevorkov [a], P. Jedrzejowski [b], M. Medraj [a,c,*]

[a] Department of Mechanical and Industrial Engineering, Concordia University, 1455 de Maisonneuve Boulevard West, QC, Montreal H3G 1M8, Canada
[b] Rolls-Royce Canada Ltd. Energy, 9545 Cote-de-Liesse, Dorval, QC, H9P 1A5, Canada
[c] Department of Mechanical and Materials Engineering, Masdar Institute, Masdar City, Abu Dhabi, P.O. Box 54224, United Arab Emirates

ARTICLE INFO

Article history:
Received 22 July 2015
Received in revised form 15 September 2015
Accepted 15 October 2015
Available online 23 October 2015

Keywords:
Water droplet erosion
TiAl alloy
Lamellar microstructure
SEM
AFM

ABSTRACT

Water droplet erosion (WDE), is a known mechanical degradation and progressive damage for turbine blades in the power generation and aerospace industries. Hence, water droplet erosion study of TiAl as an important structural material in such industries would be very attractive. The current work is to investigate the erosion damage mechanism of nearly fully lamellar Ti45Al2Nb2Mn0.8TiB_2 (45-2-2XD) alloy. This alloy was subjected to water droplet erosion using 460 μm droplets and 350 ms^{-1} impact speed. In order to track the erosion damage, WDE test was interrupted at different stages; incubation, maximum erosion rate and final steady state stages. The eroded specimens were characterized using optical microscope (OM), scanning electron microscope (SEM) and atomic force microscope (AFM). The qualitative and quantitative study reveals that the erosion damage of TiAl initiates by inhomogeneous and localized material flow followed by crack network generation on the surface. Such cracks mainly nucleate on the interlamellar slip bands and cause delamination of lamellae. Further droplet impacts result in the cracks coalescence and subsequent micro-pitting within the colonies. In the advanced stages, the erosion damage was governed by periodic water roughening and water polishing, which were observed on the bottom and the sidewalls of deep erosion craters.

1. Introduction and literature review

Liquid impingement erosion is the result of repetitive high-speed impacts of a liquid streak (jet or droplet) on a solid surface. It leads to a progressive material loss and the subsequent failure [1]. Water droplet erosion (WDE) is a practical problem in the power generation and aerospace industries where the droplets interact with the high-speed moving components. It has been known as a cause of blades degradation in the last stages of the low-pressure steam turbines [1,2]. This type of erosion is also an issue for the compressor blades of gas turbine when fog cooling system is used [1,3]. Furthermore, water droplet erosion is the main concept of plain water jet cutting process [4,5]. It has been attractive mainly for cutting of the materials that have poor machinability such as TiAl alloys [4,6].

Water droplet erosion has been studied over the past few decades and its damage mechanism, that is different from other types of erosion such as solid particle and cavitation erosions, was addressed [1,2,4,7–9]. Water hammering, stress wave generation, radial jetting and hydraulic penetration are usually described as the most destructive phenomena during the water droplet erosion [7,10]. Micro-cracking is one of the initial responses of the target and it has been argued to be a result of stress concentration around the slip steps, microstructural irregularities, and pre-existing flaws. In the case of homogenous bulk materials, localized plastic deformation and surface roughening, caused by water impacts, act as a trigger for the initiation of micro-cracks [11]. Interaction of stress waves with the microstructural irregularities and flaws, which causes stress concentration and may generate tensile stress, also contributes to micro-cracking [12]. Substantial influence of microstructural flaws on the cracking behavior and erosion performance was observed in the case of surface treated coupons such as laser nitrided Ti6Al4V [13,14] or sprayed cermet coating [15].

Water droplet erosion of the current turbine blade alloys, martensitic stainless steels and Ti6Al4V, have been studied over the years [7, 16–20]. Luiset et al. [16] described the local plastic deformation, cracking and fatigue spalling as the WDE mechanism of stainless steels. After intergranular cracking on the surface, they observed that the cracks propagate thorough the grains and result in their pulling-out and ruptures. Similar behavior was observed for erosion damage initiation of Ti6Al4V by Huang et al. [17]. They elaborated the damage initiation mechanism and highlighted the shallow depression and grains tilting as the main erosion features during the incubation of erosion. Afterwards, propagation and coalescence of these superficial cracks were reported to be the main cause for fatigue spalling and localized material loss [16,20]. Recently Kamkar et al. [19] studied the WDE damage

* Corresponding author at: Department of Mechanical and Industrial Engineering, Concordia University, 1455 de Maisonneuve Boulevard West, QC, Montreal, H3G 1M8, Canada.

http://dx.doi.org/10.1016/j.matdes.2015.10.077
0264-1275/

mechanism of Ti6Al4V at advanced stages and highlighted a periodic surface roughening and smoothing which were caused by water droplet impacts inside the erosion crater. However, such periodic roughening and smoothing were not elaborated. It is worth noting that the surface roughening by droplet impacts and formation of a jagged surface, observed for different target materials [11,21,22], was not clearly justified. In the case of TiAl alloys, the water droplet erosion damage has been rarely investigated. Kong et al. [4] studied the damage mechanism of γ-TiAl using plain water jet milling. They considered γ-TiAl as a semi-brittle material and presumed that the micro-plasticity governs its initial stage erosion. However, the micro-plastic deformation was not documented because they could not capture the early stage of erosion using water jet milling setup. Unlike the ductile metals which their damage initiation mechanism has been established [16,17,20], the erosion mechanism of TiAl intermetallic especially two phase alloys ($\alpha_2 + \gamma$) is unknown. Additionally, there is no information about the cracking behavior of these alloys during the water droplet erosion as the key contributor to the damage. It is noteworthy that the erosion damage has some similarities to the low cycle fatigue, especially, when it comes to the cracking behavior [2,7,23]. The fatigue behavior of TiAl alloys has been well studied and micro-cracking on the slip bands was highlighted as the main contributor to the damage [24–26].

Two-phase titanium aluminide alloys particularly the ones with lamellar microstructure show much better mechanical performances comparing to the alloys having monolithic microstructure of γ and α_2 constituents [6,27]. Their mechanical characteristics significantly depend on the microstructure, colony size and lamellar spacing [25,27,28]. Polycrystalline lamellar TiAl alloys comprising randomly oriented colonies deform and fracture inhomogeneously [25,29]. The deformation is mostly confined to the γ phase and not that much in α_2. In these alloys, the lamella interfaces and colony boundaries act as obstacles for crack propagation and may blunt the cracks [26,30–32]. Furthermore, the mechanical twining and the intersection of dislocations mainly at the interfaces and boundaries result in the anomalous high hardenability for these alloys [6,25]. γ/γ domain boundaries were highlighted as the key contributor to the cyclic hardening because they are the main obstacles for the motion of dislocations in the γ lamellae [25,33]. High cyclic hardening of TiAl alloys was reported as an important reason for their superior cavitation erosion performance [34] and its contribution to water droplet erosion was documented in our previous work [35]. Therein, the water erosion behavior of TiAl was compared with that of Ti6Al4V at different impact speeds. TiAl outperformed Ti64 which was attributed to its higher strength and hardenability. Water erosion performance of these two materials was reported and compared in terms of, complete erosion curves, incubation period and erosion rate. Due to space limitation, the erosion damage mechanism was not discussed in our previous paper [35].

The present paper focuses on the water droplet erosion damage mechanism of Ti45Al2Nb2Mn0.8TiB_2 (45-2-2XD), referred to as TiAl, with nearly fully lamellar microstructure. The damage initiation of TiAl alloy is investigated in-depth with respect to the local microstructure. The erosion evolution in the advanced stages is also discussed.

2. Materials and experimental procedure

2.1. Material and preparation

A Ti45Al2Nb2Mn0.8TiB_2 (45-2-2XD) plate received from Rolls-Royce Canada Ltd. has been investigated in this paper. The as-cast plate, was hot isostatically pressed (HIPped) at a pressure of 140 MPa and then annealed. The applied post treatments resulted in nearly fully lamellar microstructure of γ/α_2 laths (TiAl and Ti_3Al phases) presented at Fig. 1. Equi-axed γ grains among the randomly oriented lamellar colonies, which are the predominant constituents, can be seen in Fig. 1b. The mean size of colony and the mean lamellar spacing are 120 μm and 4.1 μm, respectively.

TiAl plate was cut based on the required dimension for the water droplet erosion test coupons. The specimen surface was grinded using SiC papers and polished by diamond vibromet polisher for 24 h (surface roughness, Ra = 0.038 μm). Then, the polished surface was subjected to the water droplet erosion.

2.2. Water droplet erosion experiments

A testing rig with rotating disk, specifically designed for water droplet erosion according to the ASTM G73 standard [36], was used in this study. It works under pressure between 30 to 40 mbar. The erosion coupons of 23 mm length, 8 mm width and 3 mm thickness were mounted on the disk and in each rotation they were subjected to the water droplet impacts. The impact angle is 90° relative to the target surface. The size distribution of generated droplets was measured using high speed camera for each nozzle. In addition, the number of droplet impacts was accurately monitored and measured in our group [37]. However, in the previous works mainly time of erosion [38] and number of impacts (rotation number) were used [19,39]. More details on the erosion rig could be found in our previous works [35,37]. In this study, the impact speed was set to 350 ms^{-1}. The erosion experiments are interrupted at different time intervals to weigh the coupon and record cumulative mass loss. Knowing the mass loss and density of tested coupon its volume loss is calculated. Hence, the relation of cumulative material loss versus erosion exposure could be established. Typical WDE performance of TiAl at impact speed of 350 ms^{-1} and droplet size of 460 μm reported by Mahdipoor et al. [35] is shown in Fig. 2a along with a schematic of the water droplet erosion process in Fig. 2b. The current paper focuses on elucidating the water erosion damage mechanism of this material. Herein, incubation, maximum erosion rate and terminal steady state stages of erosion, shown by number 1, 2 and 3 in Fig. 2a, are studied. To explore the changes happening to the sample during the incubation stage, Fig. 2a (1), the samples were

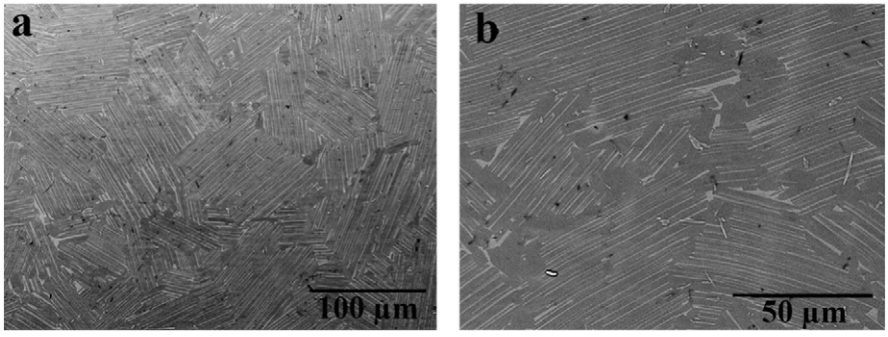

Fig. 1. SEM micrographs of TiAl alloy: (a) low magnification showing the random oriented colonies, (b) high magnification showing the lamellar microstructure.

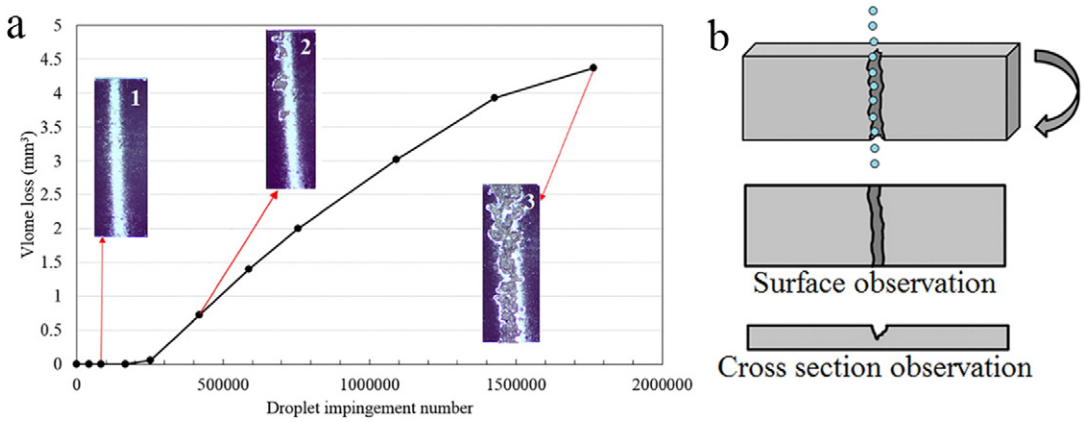

Fig. 2. (a) WDE result (cumulative material loss) of TiAl and the appearance of erosion line at different stages [35]: (1) incubation stage, (2) maximum erosion rate stage, (3) terminal steady state stage, (b) schematic of water droplet erosion process.

examined after 100,000 droplet impacts. To study the onset of material loss and the maximum erosion rate stage, Fig. 2a (2), the coupons eroded by 400,000 droplets were examined. The terminal stage of erosion, Fig. 2a (3), was investigated after 1,800,000 water droplet impacts. Although the mentioned stages were studied separately and sporadically for the erosion of other materials such as Ti6Al4V, stainless steel and WC-Co coating [16,17,19,20,22,40,41], a comprehensive study of water droplet erosion damage mechanism would be necessary for each material. Here, the evolution of cracks and fractography of eroded TiAl specimens have been examined for both the impacted surface and cross sections in the proximity of erosion lines.

2.3. Damage analysis

In order to document the erosion features, the area subjected to water droplet impacts was investigated on the surface and the cross sections (Fig. 2b). Scanning electron microscope (SEM) Hitachi S-3400N was used to study the fracture surfaces in the damaged region and monitor the cracks development. In addition, multimode atomic force microscope (AFM) was used to monitor the surface topography before and after droplet impacts (incubation stage) to document the local topography of the surface.

In order to capture sub-surface features, the cross section of eroded specimens was studied using SEM. The eroded coupons were cut using slow cutting machine with a diamond coated blade, then grinded and polished with diamond vibromet polisher. Then qualitative observation of erosion features as well as statistical analysis of cracking behavior through the cross sections of eroded coupons were performed.

3. Results and discussion

3.1. Systematic analysis of erosion damage at different stages

Water droplet erosion is a progressive and time dependent damage. Its mechanism varies at different stages of erosion. The target material response to the high speed droplet impacts and the damage mechanism at different stages are studied as following.

3.1.1. Incubation stage: microscopic observation

After 100,000 droplet impacts, the erosion experiment was stopped and the eroded coupon was explored using SEM. In the incubation period (stage 1), no clear damage or erosion features could be found macroscopically except for the change from a mirror-like to a non-reflective surface over the impacted area, as can be seen in Fig. 2a. In this stage, the erosion features were observed at high magnifications. Localized material flow can be clearly seen on the attacked surface, shown in Fig. 3a. It implies that the transition of high amounts of energy, caused by initial droplet impacts, is sufficient to activate slip systems in certain locations. It is clear that plastic deformation or material flow is notably influenced by the localized microstructure predominantly the orientation of lamella. The response of colony to mechanical loadings is known to be a strong function of its orientation with respect to the loading direction [26]. This dependency leads to anisotropic micro-plasticity, which contributes to damage initiation. Fig. 3b and c, which show the plan-view of the impinged surface, demonstrate the material flow at higher magnification. Inhomogeneous micro-plasticity within the colonies is obvious in these micrographs. Here, water droplets perpendicularly impact the target surface. The colonies, based on their orientation with respect to the droplet impact direction, demonstrate distinct responses to the impingements. They are classified in three categories; A, B, and C, which are highlighted in Fig. 3b and schematically presented in Fig. 4. Colony A shows soft mode response [26,29] where the angle between loading direction and lamellar planes is 45° ($\phi = 45$) or nearly so. It is the most favorable orientation for slip activation and plastic deformation. Here, the slip and twinning occur on {111} planes of γ layers leading to material flow parallel to the lamella interfaces, interlamellar slips [26,42]. In this orientation, the colonies do not show cyclic hardening because the γ/γ domain boundaries are not effective barriers for the motion of dislocations [6,25]. Colony B which is oriented parallel to the loading direction ($\phi = 0$) exhibits hard mode response [26,29]. In these colonies, the micro-slips and twins are mostly inclined to the lamella interfaces and the slips are called translamellar. Such colonies show strong cyclic hardening because both α_2/γ lamellar boundaries and γ/γ domain boundaries effectively prevent the motion of dislocations [6,25,26]. The third mode can be seen in colony C presenting hard and brittle behavior. There is no notable plastic deformation in this colony, as shown in Fig. 3b. Such colonies, whose lamella interfaces are almost perpendicular to the loading axis, exhibit very high yield strength [6,30]. In this case, direct cracking before fracture is expected. These three modes will be referred to in the following explanations. Here, the observed slip bands are not easily transmitted to the contiguous colonies and it is the main reason of heterogeneous plasticity. Indeed, the slip and plastic deformation are impeded by reaching the boundaries because the next colony is oriented differently, as shown in Fig. 3c. Other slip systems and potentially twins are activated in the next colonies. The features' contrast manifests that there are some extrusions mainly parallel to the lamella interfaces for the specific colonies. The extrusions are mostly the raised slip bands due to the shear deformations. It is noteworthy that the development of a severely deformed colony beside a non-deformed colony leads to local depressions and height variation near their boundaries, as shown in Fig. 3b and c.

Micro-twinning is also observed on the surface of slightly eroded TiAl alloy, as shown in Fig. 3d. In fact, high level of exerted stresses (water hammering) leads to localized crystal reorientation and

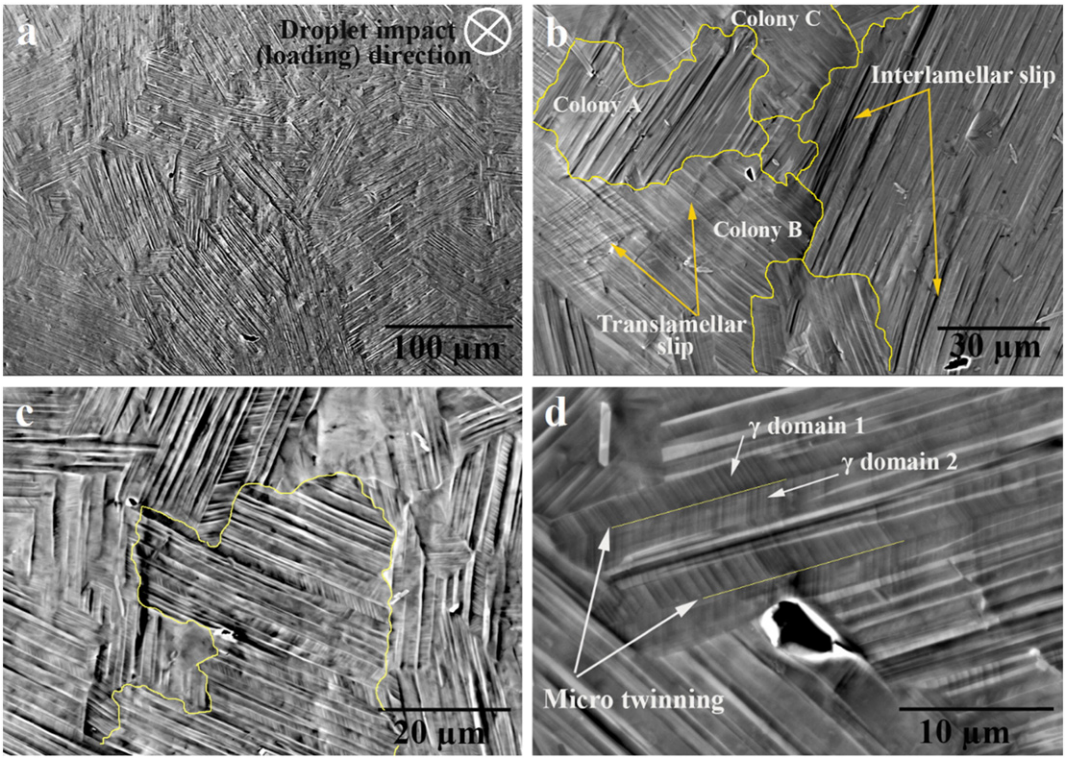

Fig. 3. SEM micrographs of slightly eroded TiAl at incubation period showing: (a) localized material flow, (b) different responses of colonies to droplet impacts, (c) slip bands impeded by colony boundaries, (d) micro-twinning within the γ layers.

formation of twinning bands within the γ layers. This reduces the level of stress concentration and partially dissipates the transmitted impact energy to the material. Further impacts thicken and raise the level of generated twinning bands. Hence, they become the potential sites for crack initiation. The contribution of twinning bands to crack initiation during the cavitation erosion of TiAl was elaborated by Howard et al. [34]. However, their formation decelerate the crack propagation because of releasing some strain energy and stress intensity in the cracks wake.

Fig. 5 depicts AFM images of original polished and slightly eroded surfaces (incubation stage). Although there is no detectable material loss in this stage, the surface topography is affected significantly by successive droplet impacts. The polished surface is relatively flat and no height variation, could be seen in the image. However, the water impinged surface exhibits perceptible contrast and height variation caused by local plastic deformations. Different levels of height variation for two adjacent colonies (A and B), shown in Fig. 5b, verifies the inhomogeneous micro-plasticity among the colonies. Moreover, the notable contrast on the boundary of colonies indicates the local depression at the interface between these two colonies. The droplet impacts during incubation stage increased the surface roughness (Ra = 0.117 μm) relative to the original polished surface (Ra = 0.038 μm). This surface roughening is responsible for the erosion damage initiation.

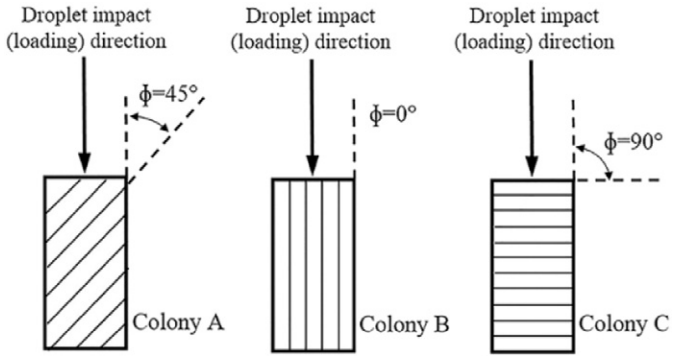

Fig. 4. Schematic of different orientation of the colonies subjected to water droplet impacts.

AFM data was processed using Bruker Nano Scope Analysis 1.40 [43] to capture the magnitude of height variations. The height profiles across a deformed colony, in two different directions, has been extracted and plotted in Fig. 6. Line 1 crosses the lamella interfaces and line 2 lies on a γ lamella and runs parallel to the interface. Thereby, the first line represents the height variation generated by interlamellar slips and the second line represents the height variation generated by translamellar slips. To elaborate the meaning of height variation along lines 1 and 2, lines 1′ and 2′ running through similar areas are demonstrated on the SEM micrograph shown in Fig. 6b. The significant height variation along line 1 indicates very high potential for cracks nucleation at the sharp notches. These stress raiser positions are mainly the α_2/γ interfaces, shown as points b_1 and d_1 in Fig. 6-(1). The cracks nucleated at these notches are interlamellar cracks and are shown over line 1′ in Fig. 6b. Such cracks were often observed in type A colonies. It is worth noting that the colony boundaries indicated by points f_1 and e_2 in Fig. 6, show relatively deep depressions. Such depressions are also shown by intense contrast of colony boundaries in Figs. 5b and 6a. The formation of these deep intrusions is function of the adjacent colonies' micro-plasticity. For instance point f_1, which looks as a deep and sharp notch, is a boundary located between two A type colonies with high level of localized material flow and interlamellar slip. Such boundary may act as a stress raiser and by further droplet impacts cause intergranular cracking.

The surface roughening in the incubation of Ti6Al4V was attributed to the tilting of grains caused by high speed droplet impacts [17]. It cannot be the case for TiAl because of its large colonies (120 μm) compared to the Ti6Al4V grains (30 μm). Also, in the case of TiAl the boundaries are often depressed all around the colonies, whilst grain tilting causes the formation of depression in one side and bump in the other side of

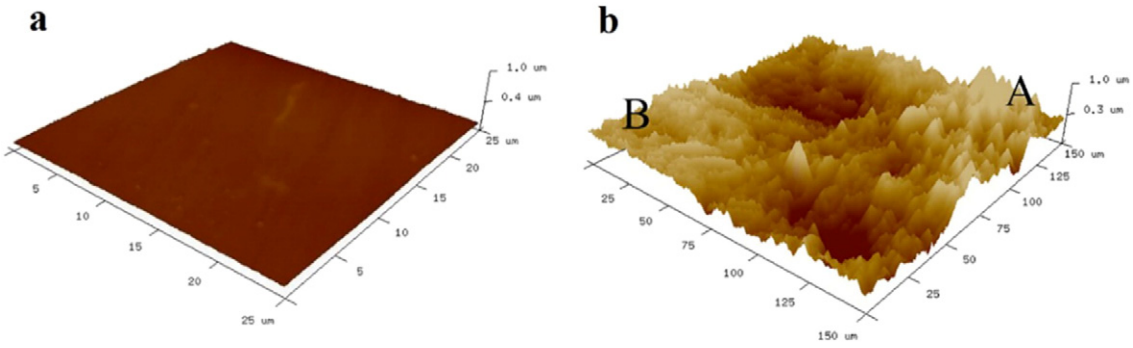

Fig. 5. AFM images of: (a) original polished surface of TiAl (b) eroded surface of TiAl after 100,000 droplet impacts.

grains [17]. Indeed, the local depression at the colony boundaries of TiAl could be attributed to the different levels of micro-plasticity for adjacent colonies.

The presented height profiles correspond to the extrusion/intrusion pattern, which is a result of shear deformation in the γ lamellae across their interfaces (referring to the points between a_1 and e_1 in Fig. 6) and parallel to their interface (raised steps between points a_2 and d_2 in Fig. 6). Here, further droplet impacts lead to high stress concentration at the sharp positions and nucleation of micro-cracks along the slip bands (interlamellar). Delamination of two adjacent lamellae accelerates the interlamellar cracking, points b_1 and d_1. An interlamellar micro-crack just nucleated at the γ/α_2 interface is shown in Fig. 7a. The hindered plastic flow by the lamellae interfaces and γ domain boundaries expedites such crack initiation. Fig. 7b exhibits the interlamellar cracks near colony boundaries where high local micro-plasticity and depression are observed, corresponding to point f_1 in Fig. 6a. It is interesting to note that the points between a_2 and d_2 indicate the raised steps either by translamellar slips or micro-twinning. These features are not as sharp as the interlamellar slip steps, which are shown by the points between a_1 and e_1. It indicates that this structure resists translamellar cracking more than interlamellar cracking.

In addition to surface cracking, a few sub-surface micro-cracks caused by stress wave propagation were observed over the weak sites of the microstructure. Fig. 7c shows an infrequent mixed translamellar/interlamellar sub-surface crack. During incubation stage, such cracks were seen mainly within the type C colonies, showing hard and brittle behavior.

3.1.2. Maximum erosion rate stage

3.1.2.1. Microscopic observation of eroded TiAl once material loss starts. After localized plastic deformation and cracks initiation, further droplet impacts result in cracks propagation, their merging and micro-voids formation. The mechanism of material loss initiation is a function of material response to the initial droplet impacts (incubation) and the erosion features generated on the surface. Upon the droplet impact, the hydrodynamic pressures (water hammering) cause local stress concentration and lead to the propagation of cracks. Further propagation results in cracks coalescence, detachment of small fragments and formation of micro-voids. This is demonstrated in Fig. 8a where two cracks running along both sides of a γ lamella at the interfaces. After reaching a certain length, they deviate into the γ lamella and meet

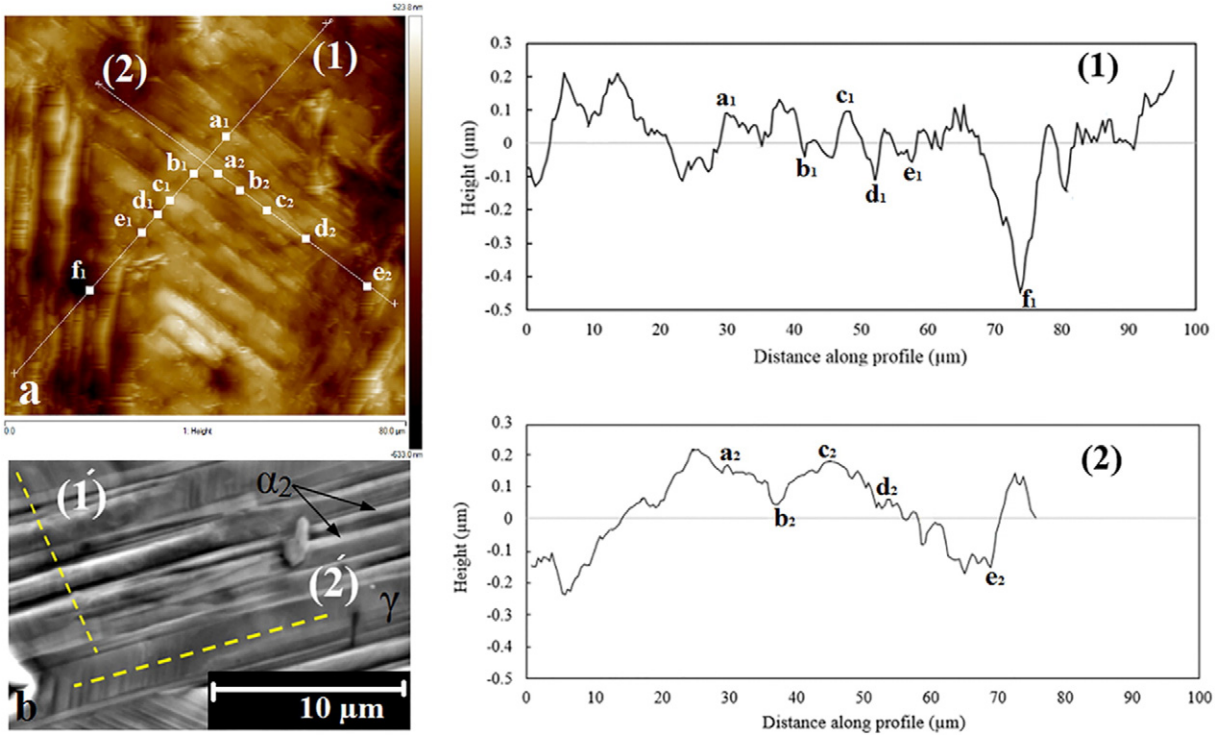

Fig. 6. (a) AFM height image of a deformed colony and extracted average height profiles along two lines (b) SEM micrograph of another deformed colony showing two lines with similar conditions.

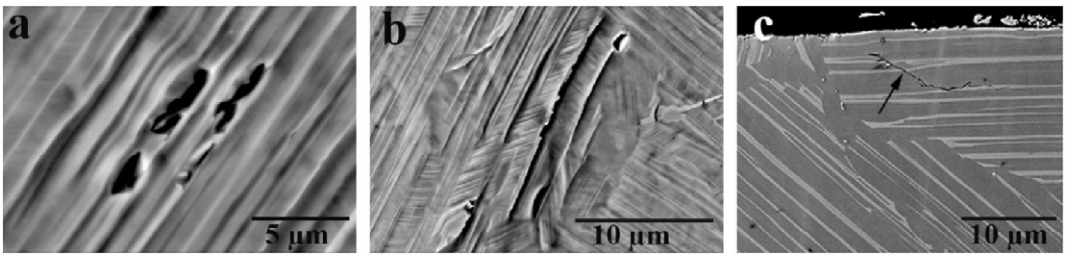

Fig. 7. (a) SEM micrograph of eroded surface showing interlamlellar cracks nucleation, (b) SEM micrograph of eroded surface showing interlamellar cracking near colony boundaries, (c) cross-sectional SEM micrograph of slightly eroded surface showing a sub-surface crack.

each other leading to a local fracture and the formation of a micro-void. The micro-voids might also be generated by high speed collision of lateral outflow jets with the raised slip bands. The speed of these jets is up to 10 times of the original droplet impact speed and they are detrimental specially when flowing on the roughened surface [44]. This type of micro-pitting mainly occurred on the lamella interfaces near the boundary of colonies as demonstrated in Fig. 8b. It is due to the high level of micro-plasticity and local depressions in these regions, as can be seen in Fig. 5b. The high stress concentration on the rim of generated micro-voids results in delamination of the lamellae. These lamellae fracture easily by the following impacts. Furthermore, water hammering and hydraulic penetration lead to crack propagation inside these micro-voids, digging their bottoms and enlarging them. In some cases, the formation of micro-voids occurred at the colony boundaries, as shown in Fig. 8c. To give a quantitative insight, twenty micro-voids in the impacted regions were considered. Out of twenty, thirteen were created within the colony and 7 were formed at the boundaries. Even the generated micro-voids at the boundaries expand towards colony interiors because of the preferential crack propagation, as shown in Fig. 8c and d. Several micro-pits are demonstrated close to each other in Fig. 8d. The micro-pit at the boundary of colonies is shown by white arrow and the ones near the colony boundaries are shown by black arrows. The successive droplet impacts result in the growth of these micro-pits and their coalescence forming relatively large and isolated crater, as presented in Fig. 9.

3.1.2.2. Microscopic observation of eroded TiAl at maximum erosion rate stage. Due to the severe plastic deformation as well as notable micro-pitting at the areas near to the colony boundaries, they become high potential sites for further damage and the formation of isolated erosion craters. Fig. 9 exhibits one of these isolated craters, which is a common feature in the maximum erosion rate stage. The irregular edges of eroded regions indicate the preferential cracks propagation which is in accordance with the brittle nature of TiAl fracture. Successive droplet impacts cause the propagation of cracks, predominantly interlamellar, both at the rim and bottom of the pits. Initially, the small fragments are removed by delamination of lamellae and their fractures within one colony, highlighted in Fig. 9. Then, water hammering and subsequent stresses cause development of opened micro-cracks. They run along the lamella interfaces in depth of the target, deviate into the lamella and continue propagating along the next interface. This track is found to be the typical cracking path and subsequent fracture among type A colonies. Another type of fracture, shown in the micrograph, is translamellar fracture. Higher level of stress intensity is required for crack propagation in this manner because the lamella interfaces blunt the propagating cracks. This type of cracking cannot only be attributed to water hammering stresses and the hydraulic penetration seems to be its main cause. Fig. 10 demonstrates the hydraulic penetration phenomenon through the cross sections of erosion craters. After merging of the generated micro-voids, a relatively wide and shallow cavity was created, shown in Fig. 10a. Initially, small fragments of

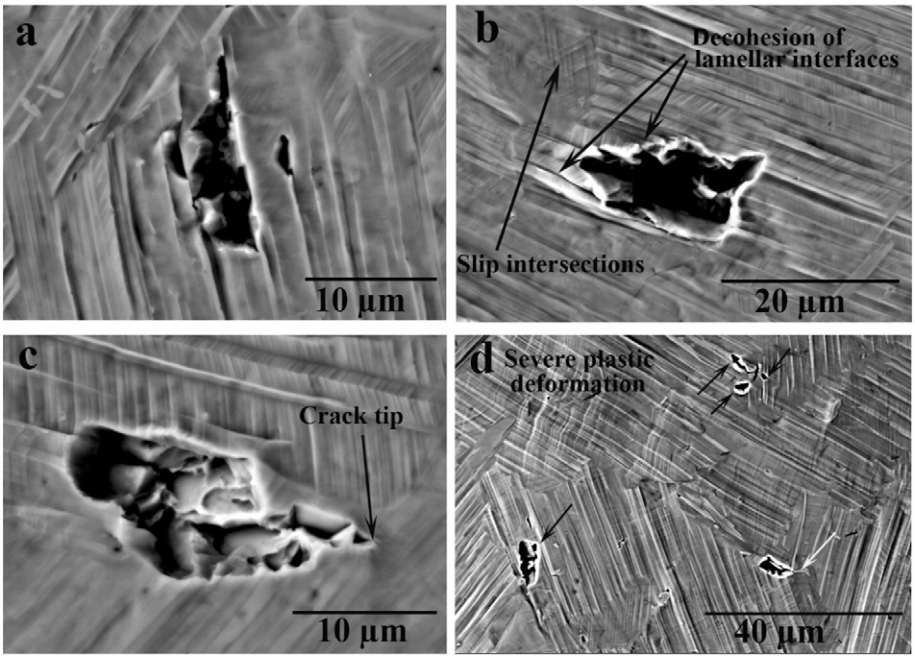

Fig. 8. SEM micrograph from eroded surface of TiAl after 400,000 droplet impacts, demonstrating severe local plastic deformation, micro-cracking and micro-pitting.

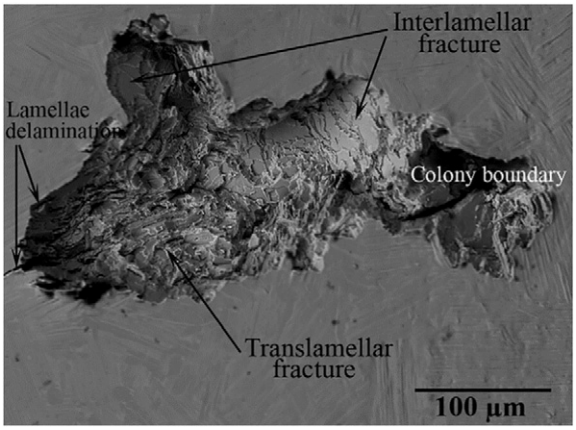

Fig. 9. SEM micrograph of an isolated erosion crater forming during the maximum erosion rate stage.

material were removed within one colony. They are associated mostly with interlamellar fractures, highlighted in Figs. 9 and 10a. Once further droplets impact directly on the cavity, water strikes its bottom in the form of spear-like central jet. This central jet forms because of shock waves coming from the sidewalls of cavity which compress the entering water and generate spear-like jet. It is the main reason of well-known phenomenon during WDE called hydraulic penetration [44], shown by arrow in Fig. 10a. The impinging droplets bore the crater and form a narrow pit at the bottom or an undercutting pit at the sidewalls of crater. An evolved tunnel is shown in Fig. 10b where the direction of water penetration is indicated by white arrows. Development of such tunnels results in the formation of undercutting pits which are significantly detrimental. The water penetration through these undercuts results in significant stress intensity, which is sufficient for translamellar fractures, highlighted in the micrograph. In this condition, the penetrated water can pull out a big chunk of material. Indeed, it results in high level of tensile stresses in the main crack wake, the direction of which is shown by the black arrows in Fig. 10b. As a result, this crack may propagate upward along the shown dashed line to reach the surface. In the lamellar TiAl alloy, the multiple micro-cracking ahead of the main crack tip, seen in Fig. 10b, may decelerate the crack growth. However, the high level of exerted stresses overcome this toughening mechanism and cause fracture. Here, the detachment of large fragments leads to the enlargement of erosion craters. This is the main reason for the observation of maximum material loss rate (erosion rate) in this stage.

3.1.3. Terminal stage

3.1.3.1. Characterization of erosion craters and damage progress. Successive water droplet impacts cause enlarging and merging of isolated erosion craters and lead to evolution of complete erosion line. Fig. 11a presents a typical erosion damage along the impingement line during the terminal stage. The width of erosion crater is 1.08 ± 0.4 mm. Unlike ductile metals which show mainly circular craters or voids [16,19], erosion craters with irregular shapes and sharp edges were observed for TiAl. Fig. 11b to e present four different cross sections of erosion line. It is clear that the depth of damage varies notably along the erosion line and it may reach 800 μm. It is due to the significant inhomogeneous cracking behavior of TiAl alloy which is function of local stress state and localized microstructure including texture and morphology. The surface pattern of erosion crater is another parameter which varies in these micrographs. A wide and relatively shallow crater with smooth surface can be seen in Fig. 11b. Such smooth surface could be roughened by droplet impacts, and form a jagged surface such as that shown in Fig. 11c. Indeed, hydraulic penetration results in the formation of small and narrow pits on the floor of cavities, and roughens the surface of erosion crater. These features play critical role in controlling material loss. The formation of jagged surface means the creation of vulnerable sites for fracture and it expedites the material loss. In addition, it influences the impact energy transmitted to the target, which is responsible for erosion damage. Herein, the evolution of generated tunnels (narrow pits) causes the formation of some deep voids (sub-surface or undercutting voids) and their adjacent weak sites, shown in Fig. 11d. The fractures of these vulnerable sites, which are usually the peaks between two adjacent tunnels or narrow voids, result in smoothing the surface. Similar behavior was reported for the erosion of Ti6Al4V [19]. In general, the evolved erosion damage inside the crater can proceed from the bottom (deepening) and the sidewalls (widening). Their progress and mechanism are reviewed below.

3.1.3.1.1. Damage progress on the bottom of erosion crater. In the evolved stages, the water droplets can reach and impinge the bottom of the crater. In this condition, water hammering, water penetration and stress waves are the main damage causes. The exerted stresses by water hammering open the micro-cracks, developed in the previous stages, and cause small detachment of material. These areas are shown by BWH (Bottom Water Hammering) in Figs. 11 and 12c. Moreover, the hydraulic penetration, explained in Section 3.1.2.2 damages the bottom of the crater. The induced stresses create a cracks network and subsequently generate tunnels, which result in water roughening. These areas are shown by BWP (Bottom Water Penetrating) in Fig. 11. Another cause of erosion damage is the stress waves propagating into the depth of target material. It may cause sub-surface crack formation which is depicted in Fig. 12a.

3.1.3.1.2. Damage progress on the sidewalls of erosion crater. Damage may proceed also on the sidewalls of the erosion craters. Upon droplet impacts, the side jetting results in water penetration and stress waves propagation laterally into the target. They are the main reasons of erosion damage on the sidewalls. The water penetration caused by side jetting occurs mostly at the corners of the erosion crater and leads to the generation of undercutting narrow pits or sub-tunnels. Such features are indicated in Fig. 11 by SWP (Sidewall Water Penetrating). Development of these pits will be followed by the removal of large fragments, shown in Fig. 11e. In addition, the successive jetting leads to stress wave propagation into the sidewalls. It results in high level of

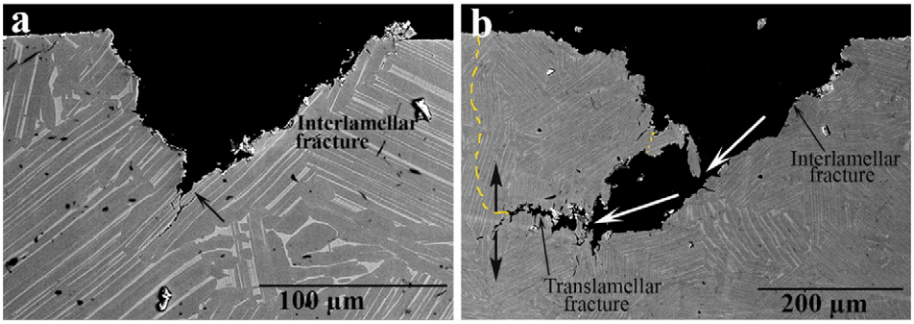

Fig. 10. Cross-sectional SEM micrographs of isolated erosion craters showing hydraulic penetration at: (a) early stage, (b) evolved stage, leading to formation of an undercutting pit.

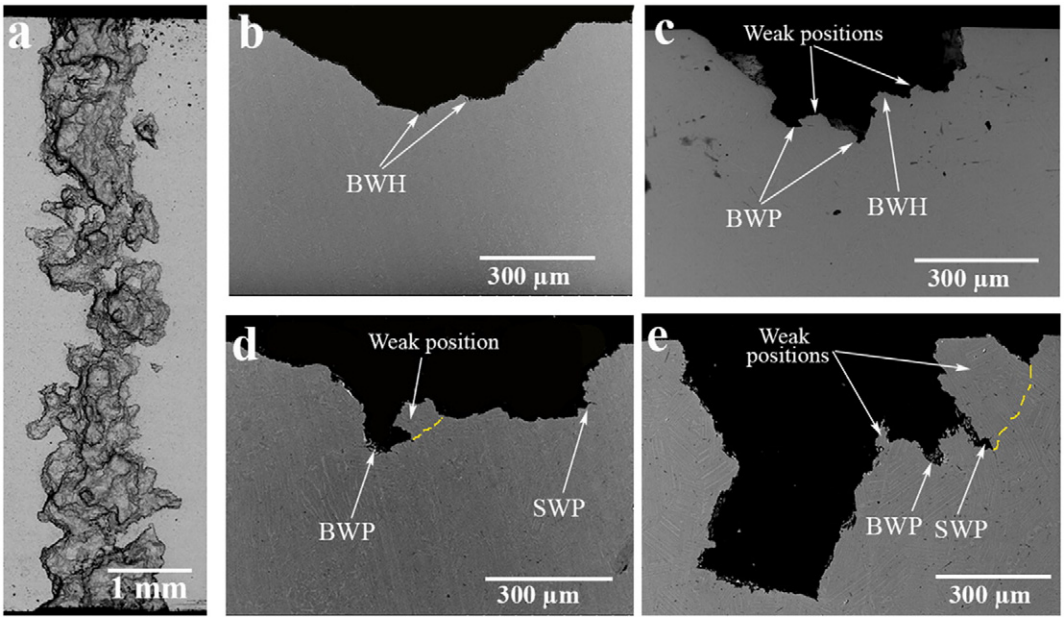

Fig. 11. (a) SEM macrograph of complete erosion damage line, (b) cross section of eroded TiAl showing wide and shallow pit with relatively smooth surface, (c) cross section of eroded TiAl showing a jagged surface, (d) cross section of eroded TiAl showing formation of an undercutting void at the bottom of crater, (e) cross section of eroded TiAl showing severe damage.

stress intensity and subsequent lateral sub-surface cracking. Despite the high level of required stress intensity for translamellar cracking, their formation near sidewalls can be observed in Fig. 12b.

3.1.3.2. Micro-analysis and fractographic interpretation of eroded TiAl at terminal stage. Cracks development is the main contributor to water droplet erosion damage. A systematic study was performed on the cracking behavior using the cross-sectional view of eroded specimens. Intergranular cracks, transgranular cracks including, interlamellar and translamellar cracks, and mixed intergranular/transgranular cracks were documented and analyzed as shown in Fig. 12. Surface and sub-surface cracks as well as crack networks can be seen over the cross sections. The interlamellar cracks were often observed and they nucleated predominantly through γ/α_2 interfaces, as shown in Fig. 12a and b. After reaching a certain length these cracks deviated into the adjacent lamella, which is called ligament bridging. The interlamellar cracks and their bridging are shown, respectively, by white and black arrows in Fig. 12a. The sub-surface cracks are formed due to the stress waves propagation, either in bottom or sidewalls of erosion craters, as shown in Fig. 12b. Fig. 12c presents the micro-cracking and fracture caused by water hammering at the bottom of a crater. It results in the removal of small fragments and it is a typical damage in type A and type B colonies. The hydraulic penetration leading to formation of a crack network and subsequent tunnel (BWP) is presented in Fig. 12d. The interlamellar cracks are the main contributor in this network; however, the hydraulic penetration on the sidewalls (SWP) is usually associated with translamellar cracking. Fig. 12e shows a crack network caused by SWP and the subsequent undercutting pit (sub-tunnel) formation. In addition, the observed intergranular crack indicates the high level of stress intensity in that region. Moreover, very long mixed cracks (interlamellar/translamellar crack shown by black arrow and intergranular/transgranular crack shown by white arrow) were observed at the bottom of another erosion crater, as shown in Fig. 12f. Formation of these long cracks are not typical cracking behavior of lamellar TiAl alloys subjected to the cyclic loading [25,26]. Besides, they were rarely seen in the case of water droplet erosion.

Crack propagation is a function of local stress state, microstructure, and material properties [25,45,46]. For instance, the preferential

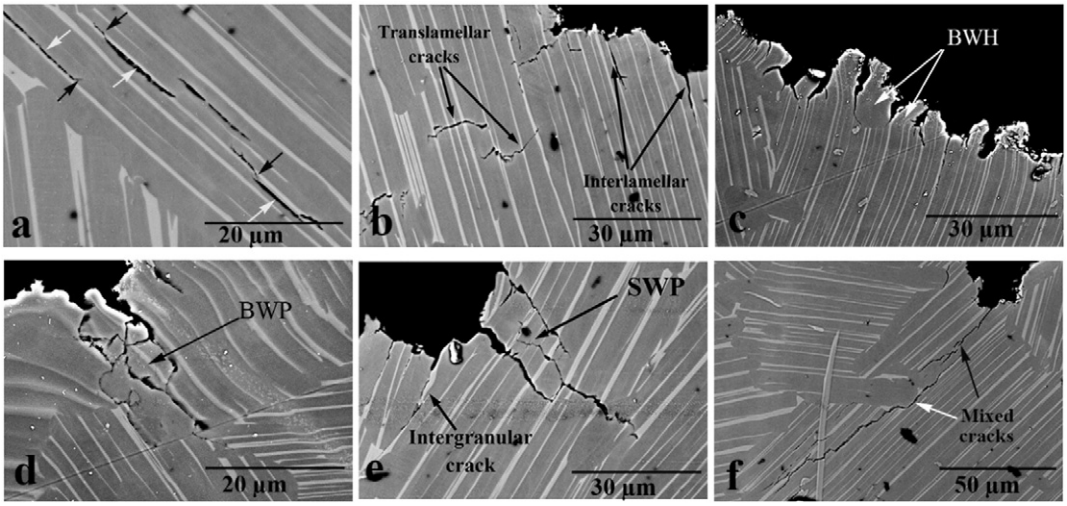

Fig. 12. SEM micrographs from cross sections of eroded TiAl at terminal stage of erosion, illustrating initiation of different types of cracks as well as their propagation and coalescence.

cracking along the rolling direction was observed over the edges of erosion craters in case of Ti6Al4V, damaged by water droplets [19]. In the case of TiAl, no general trend can be seen for cracking direction. However, the lamellar microstructure and its orientation, which is locally different, control the cracking behavior. As mentioned earlier, the colony's orientation with respect to induced loading direction is critical parameter for the localized cracking. In the advanced erosion stages and inside the erosion crater, determining the loading direction with respect to the colony's orientation is not possible. Because when the droplets impact inside the erosion crater, the hydrodynamic stresses caused by water hammering, water penetration and stress waves propagation are quite inhomogeneous. Hence, the cracking behavior could not be easily analyzed based on this parameter. High speed droplet impacts cause nucleation of different types of micro-cracks. Not all of them necessarily propagate and cause fracture, since the local stress intensity in the crack wake should be sufficient to cause propagation. For the lamellar TiAl alloys, crack propagation rate significantly depends on the local stress intensity [35], shown by large exponent for the Paris law [6]. The cracks need to reach a critical stress intensity for propagation. The γ domain boundaries, lamellae interfaces, and colony boundaries are the potential obstacles for crack propagation. The interaction of cracks and these barriers changes in different local microstructures and morphologies. In order to provide quantitative insight on dependency of erosion damage on local microstructure, more than 300 cracks were systematically studied through the cross-sectional micrographs. The number of counts for different types of observed cracks, interlamellar, translamellar, mixed interlamellar/translamellar, intergranular, mixed intergranular/transgranular, is shown in Fig. 13. It is worth noting that all of the interlamellar, translamellar, and mixed interlamellar/translamellar could be assumed as the transgranular cracks.

The large number of transgranular cracks (interlamellar, translamellar and their combination) indicates that they significantly contribute to the erosion damage. Here, the largest number of cracks is for the mixed interlamellar and translamellar which mainly cause fracture and material chipping off. The number of intergranular cracks is also notable and they need to be taken into account. In some cases, the cracks running along the colony boundaries (intergranular), deviated into the adjacent colony and generated mixed intergranular/transgranuar cracks. This combination was mainly detected at the bottom of erosion crater, as shown in Fig. 12f, where there would be the highest stress intensity. The mixed intergranular/transgranuar cracks may result in detachment of large fragments and contribute significantly to erosion damage.

Additionally, the length distribution of these cracks is presented in Fig. 14. Using cross-sectional micrographs, the length of fifty interlamellar, fifty translamellar, fifty mixed interlamellar/translamellar, thirty intergranular and thirty mixed intergranular/transgranular cracks were measured and their length distribution are presented. Almost 80% of interlamellar cracks are shorter than 10 μm and the rest are shorter than 20 μm. The wider range was observed for the translamellar cracks in which around 70% are longer than 10 μm. The length distribution of mixed cracks is the widest, from 10 to 70 μm, and they are mainly (70%) between 10 and 30 μm. These results suggest that the cracks predominantly nucleate at the lamella interfaces. Then, a crack running along the lamella interfaces deviates and bridges mainly into γ phase (translamellar) and forms a mixed crack. This bridging is known as one of the toughening mechanism of lamellar TiAl alloys [24,25]. This is clearly observed here for the eroded TiAl, shown in Fig. 12a. The bridging may occur once the interlamellar cracks reach a critical length. This critical length might be different depending on the local stress state and colonies orientation. However, the critical length should be mostly less than 10 μm, since almost 80% of interlamellar cracks are smaller than 10 μm, as shown in Fig. 14. This confirms that the larger cracks showed strong tendency to deviate into the adjacent lamellae, which generates interlamellar/translamellar cracks. On the other hand, the translamellar cracks nucleated across lamellae are normally longer than interlamellar cracks. It seems that they overcame several obstacles such as lamella interfaces to reach this length. The high level of local stress intensity is the reason for nucleation and propagation of such relatively long cracks. These cracks could either cause direct translamellar fracture or deviate into the lamella interface, form mixed and longer cracks and then fracture. Kong et al. [4] did fractography of the water jet eroded γ-TiAl alloy. They referred to the complex and heterogeneous conditions inside the erosion crater and claimed possibility of different types of fractures. However, they did not provide enough evidence to support their theories. Here, the transgranular (interlamellar and translamellar) cracks are found to be the main contributor to the fracture. Based on the number of counts for intergranular cracks and their length distribution, their contribution to the fracture and erosion damage should be notably lower. The mixed interlamellar/translamellar cracks also participate in fractures and subsequent material loss. These long mixed cracks show several ligaments in the region ahead of their tips. As a result, unstable crack growth and fracture would occur by breaking these ligaments, and lead to detachment of large fragments.

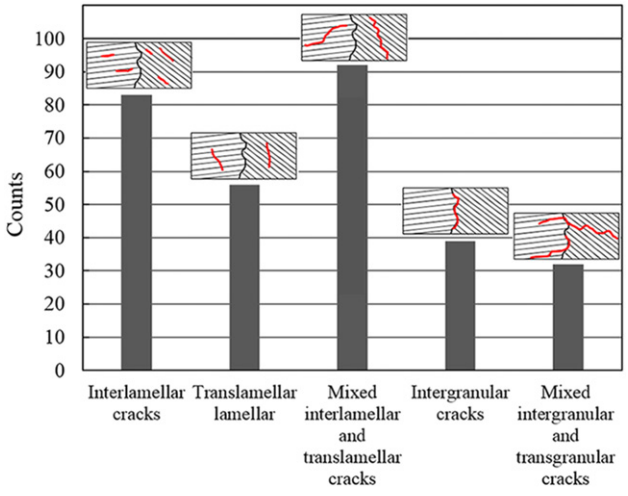

Fig. 13. Distribution of different types of cracks observed on the edges of erosion craters.

Cracks propagation and their coalescence due to the successive impacts result in localized fracture. Fractography of eroded TiAl alloy in the advanced stages of erosion was performed on the eroded surface and on the cross section. Fig. 15 illustrates cracks running along the colony boundaries which lead to intergranular fracture. Fig. 15a shows an eroded surface inside the erosion crater where the intergranular fracture surface is highlighted. Fig. 15b displays a crack propagating along the grain boundaries on a cross section micrograph. The observed cracks in this micrograph may merge and generate an intergranular fracture surface, shown by dashed line.

Fig. 16 presents two common fracture surfaces of eroded TiAl, the translamellar and interlamellar fractures. Translamellar fracture, which occurs across lamellae, was reported to occur during the fatigue of the same alloy [47]. Rough surface of the observed translamellar fracture is attributed to the high levels of stress intensity. This causes the formation of secondary interlamellar cracks, shown by black arrows, and small steps along each lamellae, shown by a white arrow. There is very high possibility for material loss in the regions having the secondary cracks. The interlamellar fractures are shown in Fig. 16b with the revealed lamella surfaces. This kind of fracture was not as frequent as translamellar fracture on the eroded regions. In Fig. 16b the fracture surface shows several steps and they are attributed to the bridging of the cracks. It seems that the short interlamellar cracks rarely caused fracture. They often deviate into the lamellae and then continue propagating along the next lamella interface, resulting in mixed cracks. These micrographs suggest that predominantly the combination of interlamellar and translamellar cracks within a colony form the fracture surfaces. The large number of mixed interlamellar/translamellar cracks

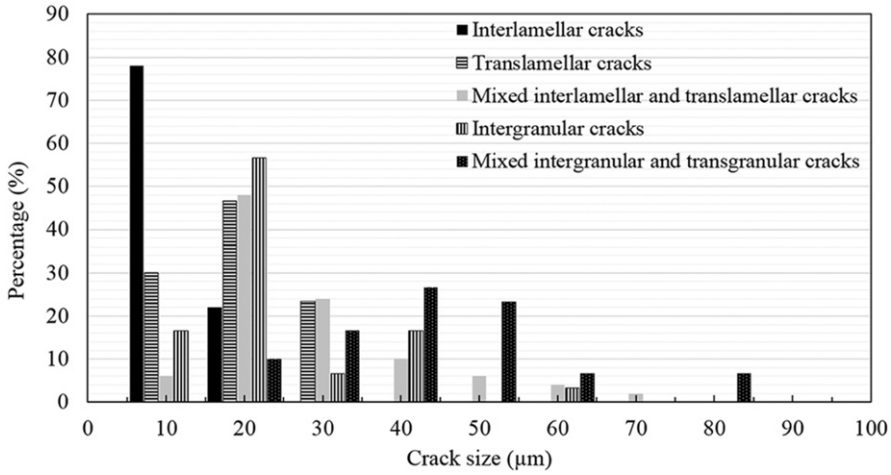

Fig. 14. Length distribution of different types of cracks observed on the edges of erosion craters.

presented in Fig. 13 is in accordance with the observed fracture surfaces. It is noteworthy that the striation marks observed on the eroded surface show the cyclic nature of water droplet erosion damage and reveal its fatigue like mechanism.

3.2. Proposed water droplet erosion mechanism for nearly fully lamellar TiAl alloy

In the present study, WDE mechanism of TiAl was investigated at both initial and advanced erosion levels. Accordingly, the damage mechanism is described for different stages including incubation, onset of material loss, maximum erosion rate and terminal stages. Since most of the micro-scale erosion features are localized along the eroded line, the influence of local microstructure on damage mechanism is also addressed.

Microscopic observation of slightly eroded TiAl revealed the initial erosion damage features. Despite the brittle nature of intermetallics, heterogeneous micro-plasticity (slip and twinning) was observed during the incubation stage. The different responses of randomly oriented colonies (with respect to the loading direction) to the initial water droplets cause inhomogeneous plasticity, cracking, and fracture. Inhomogeneous micro-plastic deformation is a known behavior during the fatigue of binary TiAl alloys [25]. In this alloy, slip mainly occurs on {111} planes parallel to the interface of γ and α_2 phases [24]. Their activation by droplet impacts in either γ matrix or γ/α_2 interfaces caused the generation of interlamellar slip steps. Translamellar slips require higher critical resolved stress since they need to overcome more obstacles including closely spaced α_2 plates. Nevertheless, they were detected over the impinged areas. This indicates that the energy of droplet impact is larger than the energy required to create translamellar slips. These fine translamellar slip bands were observed in the high strain rate fracture of TiAl alloys [24,26]. Indeed, the local transition of high amounts of energy to the target results in the activation of various slip systems in the preferential orientations. This energy could be released partially by the observed crystal reorientation and micro-twinning.

Development of micro-slip bands and micro-twins lead to creation of extrusion/intrusion patterns, shown in Fig. 17a, and followed by crack nucleation. This type of crack nucleation is called deformation-induced cracking [48] and was reported as the main contributor to crack development in lamellar TiAl alloys damaged by low cycle fatigue [25]. Herein, the generated intrusions become sharp and act as stress raisers. They result in the crack nucleation with further impacts. During the incubation of TiAl erosion, the cracks nucleated predominantly along the slip bands (intrusions), particularly interlamellar slip bands. This type of cracking was often observed in type A colonies representing soft mode. To provide a quantified insight 20 damaged colonies (within the incubation stage), which underwent slip band cracking and micro-void formation, were observed under microscope. Seventy percent of these colonies were type A showing soft mode. It proves that these colonies are more vulnerable compared to the other types and they notably contribute to the damage initiation. This vulnerability is due to their high level of experienced micro-plasticity. In type A colonies, the long and relatively easy motion of dislocations cause development of heavy extrusions and intrusions, shown in Fig. 6. The micro-cracks observed along the lamella boundaries and interfaces in such colonies, as shown in Fig. 6, support this theory. Crack propagation along the interfaces can cause delamination of two adjacent lamellae, in cases of high local stress intensity. Such cracks may run at both sides of one lamella along the interfaces. After reaching a critical length, which was

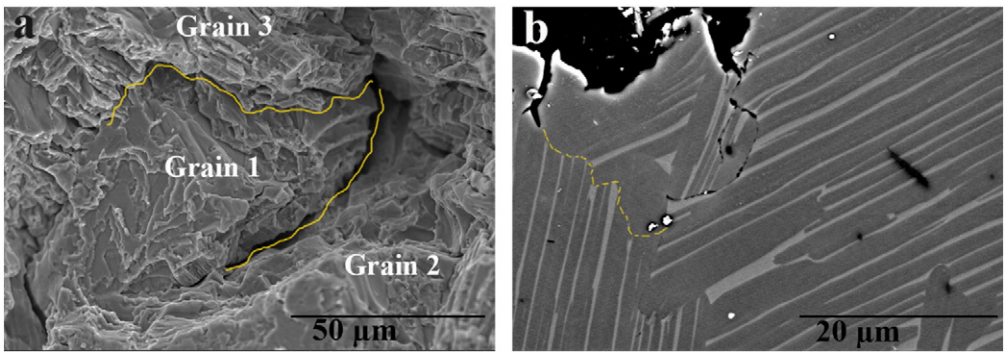

Fig. 15. SEM micrographs of eroded TiAl at terminal stage of erosion: (a) fracture surface evolved by intergranullar cracks (b) cross-sectional view showing intergranullar cracks.

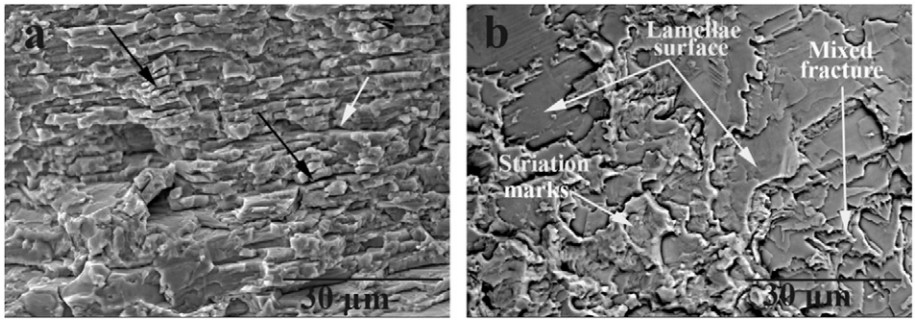

Fig. 16. SEM micrographs from the surface of eroded TiAl at terminal stage (inside the erosion craters): (a) Translamellar fracture surface, (b) interlamellar fracture surface and mixed fracture surface.

found around 10 μm, they deviate into the lamella and meet each other. This leads to a localized fracture and micro-pitting. This type of pitting is often documented near the colony boundaries and is depicted in Fig. 8. Unlike the large number of surface micro-cracks which significantly contribute to the damage initiation, sub-surface cracks were rarely observed. Only a few were documented within type C colonies, whose lamellae interfaces were almost perpendicular to the loading direction, demonstrated in Fig. 3b. They normally show high yield strength and very brittle behavior. In addition, the extrusions or raised slip steps, shown in Fig. 6, also contribute to the damage initiation mechanism. Upon droplet impingement the lateral outflow jets strike the raised slips and twinning bands, causing cracks initiation, local fracture, and micro-void formation. The contribution of extrusions to damage initiation is also inhomogeneous due to different levels of height variation among the impinged colonies. A schematic of extrusion/intrusion pattern and potential sites for cracks nucleation (intrusions), redrawn from Polak's work [49], as well as the strike of lateral outflow jets to the extrusions, redrawn from Heymann's work [44], are presented in Fig. 17.

It is noteworthy that the response of lamellar TiAl alloy to the initial droplet impacts is different from that observed for ductile metals mainly stainless steel and Ti6Al4V [11,16,17]. In the cases of ductile metals, droplet impacts predominantly cause local depressions and surface dimples. For Ti6Al4V, grain tilting, intergranular cracking and grain boundaries failure were proposed as the dominant mechanism [17]. They were not the cases for water droplet erosion of TiAl intermetallic. No dimple-like deformation was seen on the impacted surface of TiAl. However, localized severe deformation of γ phase results in micro-cracking and initial pitting along the interlamellar slip bands within the colonies.

Further droplet impacts cause more cracking and pitting in the areas, that experienced severe plastic deformation, shown in Fig. 8d. Once erosion proceeds the generated micro-voids enlarge and coalesce causing the detachment of larger fragments and the formation of isolated craters scattered along the impingement area. The craters enlargement and their merging to each other correspond to the stage showing maximum erosion rate. These craters become deeper and wider with next droplet impacts. Deepening is due to water hammering and water penetration at the bottom of crater, Fig. 10a. Widening is due to the hydraulic penetration at the sidewalls and formation of sub-tunnels and undercutting pits, Fig. 10b. Once the relatively deep and complete erosion lines formed, the material loss rate decreases corresponding to the terminal stage of erosion. Herein, the inhomogeneous stress distribution inside the erosion crater results in preferential material loss, water roughening, and formation of jagged surfaces, shown in Fig. 11c. Water roughening is associated with the generation of narrow and small pits resulting from hydraulic penetration, which bore the bottom of formed voids and craters. The exerted hydraulic stresses cause the formation of crack networks (interlamellar and tarnslamellar) and their coalescence leads to tunnel formation, shown in Fig. 12d. In some cases, the tunnels enlarge and form an undercutting void in the range of colony's size, shown in Fig. 11d. Formation of these tunnels and voids cause the generation of a jagged surface and numerous vulnerable sites. Further droplet impacts lead to the fracture of vulnerable regions and smoothing of the surface, which is referred to as water polishing. The cycle of water roughening and water polishing may occur again, if there is sufficient local stress intensity for cracks development on the freshly fractured surfaces. It is noteworthy that the attenuation of impact energy inside the deep craters and the subsequent lower local stress intensity, result in a notable decrease of crack development and material loss in the advanced stages of erosion. In addition, the trapped water inside the deep crater act as cushion and dissipate the impact energy. Also, the atomization of water droplet by hitting the sharp edges on the sidewalls of the crater may decrease the local concentration of impact energy and diminish the resulting damage or material loss. These points explain the reduction of material loss rate at the terminal stage of erosion.

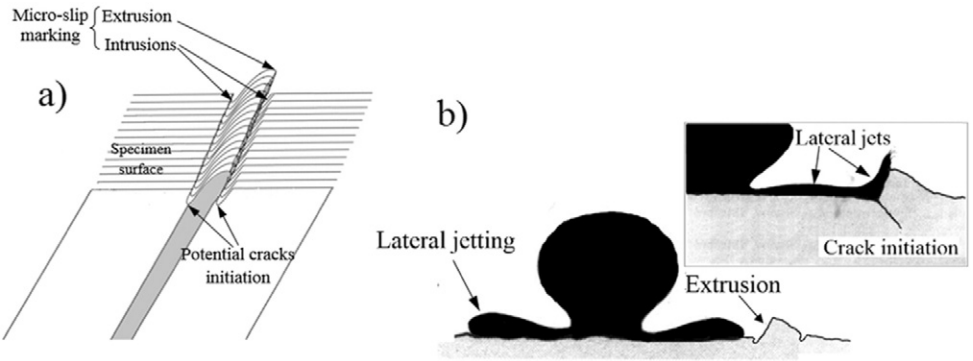

Fig. 17. Schematic of: (a) extrusion/intrusion pattern and potential sites for cracks nucleation [49], (b) high speed strike of lateral jets to the exaggerated extrusion and subsequent cracks initiation [44].

4. Conclusion

Water droplet erosion damage mechanism of the nearly fully lamellar Ti45Al2Nb2Mn0.8TiB_2 (45-2-2XD) alloy was studied. The damage features at different stages of water droplet erosion were documented. Analysis of these features revealed the following conclusions.

1. Severe and localized micro-plasticity mainly in γ phase is the initial response of the two phase (γ/α_2) TiAl alloy to water droplet impacts. This localized material flow results in the deformation-induced cracking along the lamellae interfaces. Interlamellar cracking is the dominant mechanism of damage initiation.
2. The response of lamellar colonies to droplet impingements is significantly influenced by their orientation with respect to the droplet impact direction. The colonies, oriented with 45°, show the highest level of material flow. They are the most vulnerable colonies to droplet impacts, so that 70% of cracked colonies were oriented with 45° or nearly so.
3. Inhomogeneous plastic deformation of lamellar colonies results in local depressions in the areas near to their boundaries. Numerous local and brittle fractures in such areas lead to micro-pitting and commence material loss.
4. Water hammering, water penetration and stress waves propagation are the main reasons for erosion damage in the advanced stages. They cause a periodic water roughening and water polishing on the surface of erosion craters, which governs damage progress.
5. Fractography of the eroded surface reveals that transgranular fracture consisting of the interlamellar and translamellar cracks is the main contributor to the erosion damage.

Acknowledgments

This research was carried out with support of Rolls-Royce Canada Ltd., Consortium for Research and Innovation in Aerospace in Quebec (CRIAQ MANU-419), and the Natural Sciences and Engineering Research Council of Canada (NSERC) (CRDPJ 396147-09). The authors wish to thank the help of Jie Yi, Hany Kirols, and Ahmad Omar Mostafa from Thermodynamics of Materials Group, Concordia University.

References

[1] F.J. Heymann, Liquid impingement erosion, Wear ASM Handbook, 18, ASM, 1992.
[2] G.S. Springer, Liquid Droplet Erosion, John Wiley & Sons, New York, 1976.
[3] M. Chaker, C.B. Meher-Homji, Gas turbine power augmentation: parametric study relating to fog droplet size and its influence on evaporative efficiency, J. Eng. Gas Turbines Power (2011) **133**(9).
[4] M.C. Kong, D. Axinte, W. Voice, Aspects of material removal mechanism in plain waterjet milling on gamma titanium aluminide, J. Mater. Process. Technol. 210 (3) (2010) 573–584.
[5] M. Hashish, Investigation of milling with abrasive-waterjets, J. Eng. Ind. 111 (2) (1989) 158–166.
[6] F. Appel, et al., Gamma Titanium Aluminide Alloys: Science and Technology, Wiley-VCH, Weinheim, 2011.
[7] N.L. Hancox, J.H. Brunton, The erosion of solids by the repeated impact of liquid drops, Philos. Trans. R. Soc. London, Ser. A, Math. Phys. Sci. 260 (1110) (1966) 121–139.
[8] Z. Lu, Y. Zhou, M. Zhan, An investigation of the erosion–corrosion characteristics of ductile cast iron, Mater. Des. 28 (1) (2007) 260–265.
[9] A.P. Harsha, D.K. Bhaskar, Solid particle erosion behaviour of ferrous and non-ferrous materials and correlation of erosion data with erosion models, Mater. Des. 29 (9) (2008) 1745–1754.
[10] W.F. Adler, Particulate impact damage predictions, Wear 186–187 (Part 1(0)) (1995) 35–44.
[11] G.P. Thomas, J.H. Brunton, Drop impingement erosion of metals, Proc. R. Soc. Lond. A Math. Phys. Sci. 314 (1519) (1970) 549–565.
[12] J.E. Field, ELSI conference: invited lecture: liquid impact: theory, experiment, applications, Wear 233–235 (1999) 1–12.
[13] C. Gerdes, A. Karimi, H.W. Bieler, Water droplet erosion and microstructure of laser-nitrided Ti6Al4V, Wear 186–187 (Part 2) (1995) 368–374.
[14] Z.D. Liu, X.C. Zhang, F.Z. Xuan, Z.D. Wang, S.T. Tu, In situ synthesis of TiN/Ti3Al intermetallic matrix composite coatings on Ti6Al4V alloy, Mater. Des. 37 (2012) 268–273.
[15] M.S. Mahdipoor, F. Tarasi, C. Moreau, A. Dolatabadi, M. Medraj, HVOF sprayed coatings of nano-agglomerated tungsten-carbide/cobalt powders for water droplet erosion application, Wear 330–331 (2015) 338–347.
[16] B. Luiset, F. Sanchette, A. Billard, D. Schuster, Mechanisms of stainless steels erosion by water droplets, Wear 303 (1–2) (2013) 459–464.
[17] L. Huang, J. Folkes, P. Kinnell, P.H. Shipway, Mechanisms of damage initiation in a titanium alloy subjected to water droplet impact during ultra-high pressure plain waterjet erosion, J. Mater. Process. Technol. 212 (9) (2012) 1906–1915.
[18] F.J. Heymann, A survey of clues to the relationship between erosion rate and impact parameters. Paper presented at Second Meersburg conference on rain erosion and allied phenomena, Royal Aircraft Establishment, Bondensee, Fedreal German Republic, 1967 (16–18 August).
[19] N. Kamkar, F. Bridier, P. Bocher, P. Jedrzejowski, Water droplet erosion mechanisms in rolled Ti-6Al-4V, Wear 301 (1–2) (2013) 442–448.
[20] C.R.F. Azevedo, A. Sinatora, Erosion-fatigue of steam turbine blades, Eng. Fail. Anal. 16 (7) (2009) 2290–2303.
[21] F.G. Hammitt, F.J. Heymann, Liquid erosion failures, 1975.
[22] M. Ahmad, M. Casey, N. Sürken, Experimental assessment of droplet impact erosion resistance of steam turbine blade materials, Wear 267 (9–10) (2009) 1605–1618.
[23] H. Medekshas, V. Balina, Assessment of low cycle fatigue strength of notched components, Mater. Des. 27 (2) (2006) 132–140.
[24] K.S. Chan, Y.W. Kim, Relationships of slip morphology, microcracking, and fracture resistance in a lamellar TiAl-alloy, Metall. Mater. Trans. A 25 (6) (1994) 1217–1228.
[25] K.S. Chan, D.S. Shih, Fundamental aspects of fatigue and fracture in a TiAl sheet alloy, Metall. Mater. Trans. A 29 (1) (1998) 73–87.
[26] Y. Umakoshi, H.Y. Yasuda, T. Nakano, Plastic anisotropy and fatigue of TiAl PST crystals: a review, Intermetallics 4 (Supplement 1) (1996) S65–S75.
[27] S. Kim, J. Hong, Y. Na, J. Yeom, S. Kim, Development of TiAl alloys with excellent mechanical properties and oxidation resistance, Mater. Des. 54 (2014) 814–819.
[28] K.S. Chan, Y.W. Kim, Effects of lamellae spacing and colony size on the fracture resistance of a fully-lamellar TiAl alloy, Acta Metall. Mater. 43 (2) (1995) 439–451.
[29] H. Jiang, F.A. Garcia-Pastor, D. Hu, X. Wu, M.H. Loretto, M. Preuss, P.J. Withers, Characterization of microplasticity in TiAl-based alloys, Acta Mater. 57 (5) (2009) 1357–1366.
[30] H. Inui, M.H. Oh, A. Nakamura, M. Yamaguchi, Room-temperature tensile deformation of polysynthetically twinned (PST) crystals of TiAl, Acta Metall. Mater. 40 (11) (1992) 3095–3104.
[31] P. Wang, N. Bhate, K.S. Chan, K.S. Kumar, Colony boundary resistance to crack propagation in lamellar Ti–46Al, Acta Mater. 51 (6) (2003) 1573–1591.
[32] S. Yokoshima, M. Yamaguchi, Fracture behavior and toughness of PST crystals of TiAl, Acta Mater. 44 (3) (1996) 873–883.
[33] Z.W. Huang, P. Bowen, Localised cyclic plastic deformation on translamellar fracture surfaces in a P/M–TiAl-based alloy, Acta Mater. 47 (11) (1999) 3189–3203.
[34] R.L. Howard, A. Ball, Mechanisms of cavitation erosion of TiAl-based titanium aluminide intermetallic alloys, Acta Mater. 44 (8) (1996) 3157–3168.
[35] M.S. Mahdipoor, H.S. Kirols, D. Kevorkov, P. Jedrzejowski, M. Medraj, Influence of impact speed on water droplet erosion of TiAl compared with Ti6Al4V, Sci. Report. 5 (2015) 14182, http://dx.doi.org/10.1038/srep14182.
[36] ASTM Standard G73, 2010, Standard test method for liquid impingement erosion using rotating apparatus, ASTM International, West Conshohocken, PA, 2010, http://dx.doi.org/10.1520/G0073-10www.astm.org.
[37] H.S. Kirols, D. Kevorkov, A. Uihlein, M. Medraj, The effect of initial surface roughness on water droplet erosion behaviour, Wear 342 (2015) 198–209.
[38] J.M. Robinson, R.C. Reed, Water droplet erosion of laser surface treated Ti–6Al–4V, Wear 186-187 (2) (1995) 360–367.
[39] R.K. Nalla, B.L. Boyce, J.P. Campbell, J.O. Peters, R.O. Ritchie, Influence of microstructure on high-cycle fatigue of Ti–6Al–4V: bimodal vs. lamellar structures, Metall. Mater. Trans. A Phys. Metall. Mater. Sci. 33 (13) (2002) 899–918.
[40] P.H. Shipway, K. Gupta, The potential of WC-Co hardmetals and HVOF sprayed coatings to combat water-droplet erosion, Wear 271 (9–10) (2011) 1418–1425.
[41] N. Kamkar, et al., Water droplet impact erosion damage initiation in forged Ti–6Al–4V, Wear 322–323 (2015) 192–202.
[42] Y. Umakoshi, H.Y. Yasuda, Y. Nakano, The effect of orientation and lamellar structure on the fatigue behaviour of TiAl PST crystals, Proceedings of 2nd International Conference on Fundamental Physical Aspects of the Strength of Crystalline Materials, 21–26 Aug. 1994, Japan Inst. Metals, Sendai, Japan, 1994.
[43] *Nanoscaleworld.bruker-axs.com/nanoscaleworld/media/p/775.aspx*. [cited 17/06/2015].
[44] F.J. Heymann, Erosion by Liquids, 1970.
[45] J. Zhang, X. Cheng, Z. Li, Total fatigue life prediction for Ti-alloys airframe structure based on durability and damage-tolerant design concept, Mater. Des. 31 (9) (2010) 4329–4335.
[46] A.L. Dowson, M.D. Halliday, C.J. Beevers, In-situ SEM studies of short crack growth and crack closure in a near-alpha Ti alloy, Mater. Des. 14 (1) (1993) 57–59.
[47] J. Yang, H. Li, D. Hu, M. Dixon, Microstructural characterisation of fatigue crack growth fracture surfaces of lamellar Ti45Al2Mn2Nb1B, Intermetallics 45 (2014) 89–95.
[48] Z.W. Huang, P. Bowen, Persistent microslip bands in the lamellar TiAl structure subjected to room temperature fatigue, Scr. Mater. 45 (8) (2001) 931–937.
[49] J. Polak, J. Man, Mechanisms of extrusion and intrusion formation in fatigued crystalline materials, Mater. Sci. Eng. A 596 (2014) 15–24.